Crystallization Pathways of Iron Formations: Insights From Magnetic Properties and High-Resolution Imaging of the 2.7 Ga Carajás Formation, Brazil

Livia Teixeira, Julie Carlut, Siciliano Rego, Ricardo I F Trindade, Pascal Philippot

Geobiology

WILEY

gebiology

ORIGINAL ARTICLE OPEN ACCESS

Crystallization Pathways of Iron Formations: Insights From Magnetic Properties and High-Resolution Imaging of the 2.7 Ga Carajás Formation, Brazil

Livia Teixeira[1,2,3] | Julie Carlut[2] | Eric Siciliano Rego[4] | Ricardo I.F. Trindade[1] | Pascal Philippot[3]

[1]Departamento de Geofísica, Instituto de Astronomia, Geofísica e Ciências Atmosféricas, Universidade de São Paulo, São Paulo, Brazil | [2]Université Paris Cité, Institut de Physique du Globe de Paris, CNRS UMR-7154, Paris, France | [3]Géosciences Montpellier, CNRS, Université de Montpellier, Montpellier, France | [4]Geosciences Research Division, Scripps Institution of Oceanography, UC San Diego, La Jolla, California, USA

Correspondence: Livia Teixeira (liviateixeira@usp.br)

Received: 2 May 2024 | **Revised:** 25 November 2024 | **Accepted:** 26 November 2024

Funding: This work was supported by Fundação de Amparo à Pesquisa do Estado de São Paulo (Grant/Award Number: 2021/10949-4, 2019/12132-5 and 2015/16235-2).

Keywords: Carajás | iron formations | magnetite crystallization | Neoarchean | rock magnetism | Verwey transition

ABSTRACT

Banded iron formations (BIFs) are chemical sedimentary rocks commonly utilized for exploring the chemistry and redox state of the Precambrian ocean. Despite their significance, many aspects regarding the crystallization pathways of iron oxides in BIFs remain loosely constrained. In this study, we combine magnetic properties characterization with high-resolution optical and electron imaging of finely laminated BIFs from the 2.7 Ga Carajás Formation, Brazil, to investigate their nature and potential for preserving ancient environmental conditions. Our findings reveal that magnetite, in the form of large 0.1–0.5 mm crystals, is the main iron oxide, with an overall averaged saturation magnetization (M_s) of 25 Am^2/kg (corresponding to ~27 wt% of magnetite) over the studied 230 m of the sequence. Nevertheless, the non-negligible contribution of minerals with higher coercivity suggests variable proportions of hematite along the core. Additionally, we observe non-uniform behavior in magnetite grains, with distinct populations identified through low-temperature measurements of the Verwey transition. Petrographic observations indicate that the original sediment was an Fe–Si mud consisting of a ferrihydrite–silica mixture formed in the water column. This assemblage was rapidly transformed into nano-scale hematite embedded in silica as indicated by a honeycomb structure composed of Si-spherules distributed in a microscale hematite matrix. Textural relationships show that the nucleation of magnetite started during or soon after the formation of hematite, as indicated by the preservation of the Si-spherules within magnetite cores. Further magnetite overgrowth stages are characterized by inclusion-free rims, associated with continuous Si supply during the evolving diagenetic or early metamorphic stages. These findings, combined with existing literature, suggest that ferrihydrite precipitated alongside Si and organic material, later crystallizing as hematite on the seafloor. Anaerobic respiration by Fe(III)-reducing microorganisms likely contributed to early magnetite formation in a fluid-saturated, unconsolidated sediment. Subsequent low-grade metamorphism and Si mobilization led to palisade quartz precipitation and a second stage of magnetite growth likely formed at the expense of matrix hematite through thermochemical Fe(III) reduction. Low-temperature magnetic analyses revealed that the two generations of magnetite core and rim are associated with specific stoichiometry.

1 | Introduction

Banded iron formations (BIFs) are considered one of the best-preserved archives of Precambrian seawater (see Konhauser et al. 2017 for a review). BIFs are characterized by alternating layers of Fe-rich and Si-rich minerals at scales ranging from submillimeter (sub-mm) microbands to meter-scale macrobands (Trendall 2002). Banded micritic IF layers are typically composed of fine-grained material (i.e., micritic texture termed ferhythmites by Beukes and Gutzmer (2008), interpreted to have formed in deep, low-energy marine environments. The canonical model for the formation of these chemical sediments relies on the oxidation of soluble dissolved ferrous iron [Fe(II)] and precipitation of insoluble Fe(III) oxyhydroxide phases (Cloud 1973). Among the different Fe^{2+} oxidation pathways are those involving O_2-induced oxidation by photosynthetic bacteria (Cloud 1973) or chemolithoautotrophic species when only a limited amount of oxygen produced by photosynthetic bacteria is available (Konhauser et al. 2002; Smith, Beukes, and Gutzmer 2013; Smith and Beukes 2023), photo-oxidation by UV light (Cairns-Smith 1978; Braterman, Cairns-Smith, and Sloper 1983; Nie, Dauphas, and Greenwood 2017), and/or Fe(II) oxidation by anoxygenic photosynthesis (Konhauser et al. 2002; Kappler et al. 2005). Alternatively, additional lines of evidence have argued that the primary mineralogy of BIFs comprised Fe(II) hydrous silicates, such as greenalite, which underwent post-depositional oxidation to form Fe(III) oxides and mixed valence silicates (Rasmussen, Krapež, and Meier 2014; Rasmussen, Muhling, and Krapež 2021; Johnson et al. 2018; Tosca, Guggenheim, and Pufahl 2016). While debate continues on the primary mineralogy of BIFs, evidence of both ferric and ferrous minerals, including mixed valence Fe minerals like magnetite [$Fe(II)Fe(III)_2O_4$], supports the notion that the presence of Fe(II) in BIFs could result from early or late diagenetic reduction of Fe(III) during organic matter oxidation. This reduction can occur through processes such as microbial dissimilatory Fe(III) reduction (DIR) or be induced by reaction during burial heating (Konhauser, Newman, and Kappler 2005; Heimann et al. 2010; Craddock and Dauphas 2011; Halama et al. 2016). Significantly, a strong argument supporting the role of microbial reduction mechanisms in BIFs is the presence of highly negative $\delta^{13}C_{org}$ values, which are consistent with the consumption of organic carbon by DIR bacteria during the reduction of Fe(III) (Konhauser, Newman, and Kappler 2005; Heimann et al. 2010; Smith, Beukes, and Gutzmer 2013; Smith and Beukes 2023).

Despite magnetite and hematite being recognized as the most prominent magnetic minerals found in BIFs, only a few studies have applied rock magnetic properties, such as remanence analysis and the anisotropy of magnetic susceptibility, to elucidate the mechanisms of BIF genesis (Schmidt and Clark 1994; Tompkins and Cowan 2001; Sumita et al. 2001; Carlut et al. 2015). The magnetic properties of these mineral assemblages allow for the characterization of variations in composition, concentration, and grain size of iron oxides (Evans and Heller 2003).

To explore the potential of magnetic properties in unraveling the crystallization pathways behind hematite and magnetite formation, and to evaluate if the Carajás BIFs reflect the primary nature of the first precipitates or the products of post-depositional alteration under diagenetic conditions, we developed a multi-proxy analytical approach combining optical and high-resolution electron imaging techniques with magnetic properties measurements applied to a selection of pristine samples collected over a 230-m-long drill core that intercepted the Neoarchean (2.74 Ga old) BIF and associated carbonates of the Carajás Mining Province, located in the Amazon Craton, Brazil. Our results identified different generations of magnetic grain populations and a variety of textural relationships that offered insights on the relative sequence of crystallization and possible mechanisms of BIFs and chert formation. Our dataset, along with the Fe isotope data recently published for the same samples (Rego et al. 2021), enables us to explore a potential scenario for the crystallization of BIFs. In this scenario, a portion of the ambient hydrothermally derived Fe(II) undergoes oxidation to Fe(III) via anoxygenic photosynthesis in the water column to form cell-like ferrihydrite in association with aqueous silica and organic compounds. This assemblage was subsequently deposited on the seafloor to be pseudomorphed into nano-scale hematite and microcrystalline quartz forming spherule-like features. A first generation of magnetite formed via DIR occurred during or soon after hematite–microquartz pseudomorphosis. A late diagenetic and/or low-grade metamorphic stage of pervasive silica mobilization leading to palisade quartz formation was accompanied by a second stage of magnetite growth possibly through thermochemical Fe(III) reduction.

2 | Geological Setting

The Carajás Mineral Province (CMP) located in the southeastern portion of the Amazon Craton, Pará State (Brazil, Figure 1) exhibits world-class BIFs and Mn, Cu, and Au deposits (Klein and Ladeira 2002). The Carajás Basin, which is part of the CMP, consists of a Meso- to Neoarchean basement composed of mafic granulites, migmatites, and metavolcanic rocks that is unconformably overlain by Neoarchean and Paleoproterozoic volcano-sedimentary successions of the Itacaiúnas Supergroup (Machado et al. 1991; Rosière et al. 2006).

The Itacaiúnas Supergroup includes the Grão Pará Group, which is subdivided into the Parauapebas Formation, dominated at its base by ~2750 Ma basaltic rocks (Machado et al. 1991; Trendall et al. 1998; Martins et al. 2017) which are conformably covered by the Carajás Formation (Martins et al. 2017; Rossignol et al. 2022). The Carajás Formation is a 200- to 300-m thick succession predominantly composed of BIFs with minor black shale, conglomerate (Cabral et al. 2013, 2017), and carbonate (Rego et al. 2021), reflecting a range of depositional environments from shallow water, high-energy environments to deep and quiet water settings (Tolbert et al. 1971; Lindenmayer, Laux, and Teixeira 2001; Macambira and Schrank 2002; Ribeiro da Luz and Crowley 2012; Rossignol et al. 2022, 2023). The age of BIF deposition is well constrained by U–Pb zircon dates obtained in the Parauapebas basalts (2755–2740 Ma; Gibbs et al. 1986; Krymsky et al. 2007; Machado et al. 1991; Martins et al. 2022), a possible tuff horizon (2743 ± 11 Ma), and a dolerite dike intersecting the Carajás Formation (2740 ± 8 Ma; Trendall et al. 1998). In addition, Rossignol et al. (2022) reported a detrital

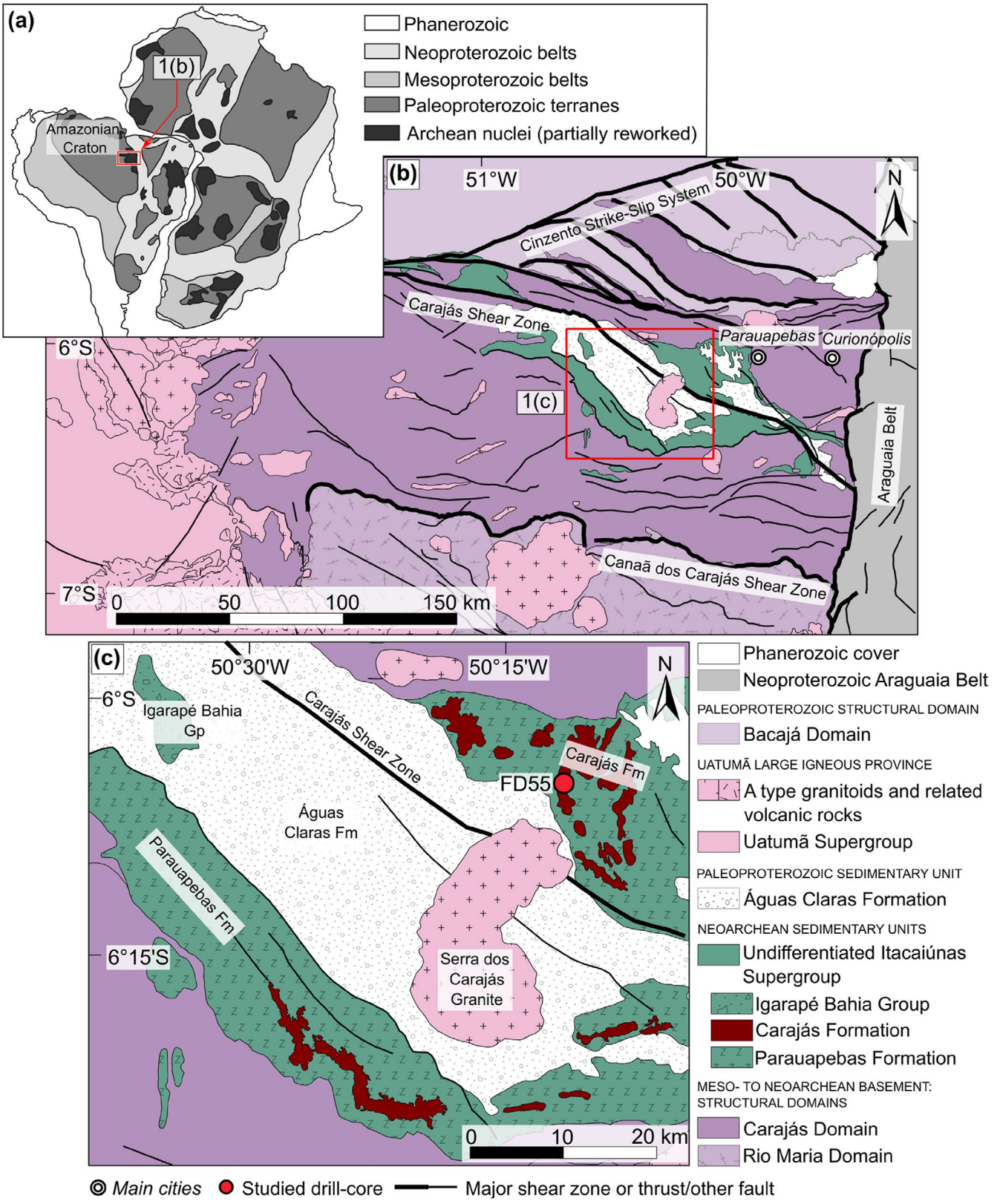

FIGURE 1 | Geological map showing Amazonian Craton and the Carajás Mineral Province. (a) Reconstruction of the main tectonic block; (b, c) simplified map of the Carajás Basin and the location of the studied drill core (adapted from Rossignol et al. 2023).

zircon maximum age of 2720 ± 6 Ma extracted from volcaniclastic samples from the Carajás Formation, and Cabral et al. (2013) reported two Re-Os ages of 2661 ± 110 and 2710 ± 38 Ma in black shales intercalated with BIFs.

In terms of stratigraphic classification, the unprecedented europium anomalies (Eu/Eu* up to 18) reported by Rego et al. (2021) make the classification of the Carajás BIFs more consistent with that of Algoma-type BIFs (Huston and Logan 2004). However,

as Martins et al. (2022) pointed out, in terms of lateral extent and thickness, the Carajás BIFs—with over 250 km in length and 100 km in width (Justo et al. 2020), and approximately 400 m in thickness (Martins et al. 2022)—greatly exceed the expected definitions for Algoma-type BIFs.

3 | Materials and Methods

3.1 | Samples

Samples analyzed in this study are from the well-preserved drill core FD55 of the N4 zone, Serra Norte mining district (Figure 1c). This core was made available by Vale S.A. and has been previously described and investigated for its sedimentology, mineralogy, major and trace element concentrations, and Fe isotope compositions by Rego et al. (2021, 2023) and Rossignol et al. (2023). Core FD55 intercepts pristine and finely laminated BIFs up to 300 m in thickness, interlayered with 2 m of carbonate horizons that conformably overlie well-preserved amygdaloidal basalts of the Parauapebas Formation (Figures 1c and 6). The BIFs consist of mm- to cm-scale laminae of metallic-gray magnetic-rich layers alternating with chert (microcrystalline quartz) and jasper (i.e., association of microcrystalline hematite and quartz with local magnetite, see below). Local dark to greenish ankerite- and magnetite-rich layers are also present. The two main carbonate horizons located at the base of the core are formed of Fe-poor carbonates composed of calcite, ankerite, and minor magnetite that progressively evolves towards a more Fe-rich composition at the contact with the underlying and overlying BIFs (Rego et al. 2021). The Fe-rich carbonates consist dominantly of ankerite and chert intercalated with magnetite layers.

3.2 | Mineralogy

A total of 53 polished petrographic thin sections were examined using an optical Zeiss AX10 microscope from the Institut de Physique du Globe de Paris (IPGP). Both transmitted and reflected light were used. Based on these observations, four samples were selected (FD55-349.06, FD55-352.00, FD55-384.43, and FD55-463.50 m depth) for in-depth scanning electron microscopy (SEM) investigations. High-resolution images and semi-quantitative composition were obtained using a Zeiss EVO MA10 SEM and a Zeiss AURIGA 40 FEG-FIB-SEM equipped with Brucker XFlash-410-M EDS detectors, available within the PARI analytical platform at IPGP. Observations were performed on samples coated with a 10 nm thick carbon layer, in backscattered electron (BSE) mode, using 15 kV as accelerating voltage and working distances ranging from 8.5 to 13 mm.

Mineral identification was further conducted using rock powders. Approximately 100 samples were initially cut with a diamond saw, then fragments of rocks weighting between 2 and 5 g were crushed using an agate mortar, and finally pulverized in a Retsch PM200 planetary ball mill at a speed of 400 rpm for 30 min per sample. After each round, the mortar, grinding jar, and balls (all made of agate) were cleaned by pulverizing fine silica sand grains, followed by a thorough rinse with Milli-Q water. Compressed air was then used to speed up the drying process of both the mortar/jars and the balls.

Powder X-ray diffraction analysis was performed on approximately 50 mg of selected 15 samples at room temperature using the PANalytical X'Pert Pro at the Chemistry department of Université Paris Cité. The diffractometer was equipped with a cobalt (Co) K alpha radiation source and a PIXcel multi-channel detector in linear 1D mode, with an active angular range of 2.122°. Fixed divergent slits and anti-scatter slits were used on the incident beam path. Measurements were conducted at 40 kV and 40 mA, covering a range from 5° to 70° in 2θ, with a step size of 0.017°. The resulting diffractograms were processed and interpreted for mineral identification using the Match! Software (Crystal Impact, Bonn, Germany), from which the relative quantity of each mineral (in percentage) was determined through Rietveld refinement.

3.3 | Rock Magnetism

Ninety-two levels, comprising BIFs and the Fe-carbonate facies, along the entire length of the core, were selected for rock magnetic measurements. Rock powders were encapsulated in transparent, hard gelatin capsules (Size 5) supplied by LGA (Laboratoires des Gélules et des Azymes), each containing approximately 20 mg of material for hysteresis measurements. About 100 mg of powder was kept for thermomagnetic measurements. Hysteresis parameters (saturation magnetization—M_s, saturation remanent magnetization—M_{rs}, coercivity—H_c, and coercivity of remanence—H_{cr}) and isothermal remanent magnetizations (IRMs) were measured using a vibrating sample magnetometer (μ-VSM) from Princeton Measurements Corporation at the Mineral Magnetism Analytical Facility of IPGP-IMPMC (Institut de Minéralogie, de Physique des Matériaux et de Cosmochimie). The measurement parameters for hysteresis were field up to 1 T, averaging measurement time 100 ms, field increments 5 mT, and 1 mT for backfield measurements (H_{cr}). In order to estimate the amount of high coercivity minerals (i.e., hematite), hard IRM (HIRM, Liu et al. 2007) and S-ratio (Bloemendal et al. 1992) were calculated using IRM acquisitions performed on the same instrument with increasing and decreasing induced field following a linear distribution of the field steps.

To further characterize the magnetic mineralogy, thermomagnetic experiments (variation of magnetic susceptibility as a function of temperature) were conducted on selected depths using the AGICO KLY-3 Kappabridge (and CS-3 Temperature Control Unit). Samples were cooled to a temperature of −192°C and then slowly warmed to room temperature. The samples were then heated up in a steady flow of argon to a peak temperature of 700°C and then cooled down to 40°C. Each cooling–heating cycle is accompanied by changes in magnetic susceptibility allowing to characterize magnetic minerals (Tauxe 2010). One of these magnetic transitions is the Verwey transition (T_V) of magnetite, which, for stoichiometric magnetite, is observed at ~120 K. Variations in the peak distributions of Verwey transition are commonly attributed to the influence of factors such as cation substitution, oxidation effects, or biogenicity (Chang et al. 2015; Jackson and Moskowitz 2021 and references therein).

Another transition is the Curie temperature which is around 580°C for magnetite and 680°C for hematite. The transition temperatures were estimated using the first derivative of the thermomagnetic curves (Tauxe 2010).

The behavior of the low-temperature transitions was further studied by measuring the remanent magnetization of five samples using a Quantum Design Magnetic Properties Measurement System (MPMS). The samples were cooled from 300 K down to 10 K in a zero-field environment (i.e., zero-field-cooled, ZFC) and then, as the samples returned back to room temperature, they were cooled down again in the presence of a 2.5-T field (field-cooling, FC). While the samples were progressively heated up from 10 K to room temperature in a 0 T field, the magnetic moment was measured every 5 K or every 2 K (between 80 and 150 K) to cover the T_V range in detail. The magnetic moment (M) was then normalized by mass and the first derivative of M with respect to temperature was calculated for the ZFC curve to estimate T_V. To evaluate the state of the magnetic domain of the grains, the ratio R_{LT} was also calculated as (Equation 1) (Smirnov 2009):

$$R_{LT} = \frac{M_{fc}(20K)}{M_{zfc}(20K)} \quad (1)$$

4 | Results

4.1 | Mineralogical and Petrographic Data

4.1.1 | Macroscopic Observations

The four thin sections inspected by SEM (FD55-463.50, FD55-384.43, FD55-352.00, and F55-349.06) represent the different morphologies of layering, mineral textures, and the relative proportions of Fe-oxides, Fe-carbonates, and silica in the BIFs sequence; illustrating the different stages of the depositional and diagenetic history experienced by the rocks. FD55-463.50 and FD55-384.43 consist of finely laminated BIFs comprising 0.2–2 mm thick microbands of dark to metallic-gray Fe-oxides (e.g., magnetite and hematite) alternating with ferruginous beds composed of microcrystalline hematite and quartz, and some magnetite (Figure 2a,b). Laminations can exhibit an even banding (Figure 2b) but locally show wavy structures and erosion surfaces (Figure 2a). Samples FD55-352.00 and F55-349.06 (Figure 3a,e) present relatively large (mm to cm thick) zones of jasper, chert, and/or magnetite-rich domains displaying lateral thickness variations, which seems to overprint the original, regular, and finely laminated texture mainly underlined by magnetite layers. In addition, carbonates (e.g., calcite and ankerite), phyllosilicates (stilpnomelane), and rare euhedral pyrites occur randomly disseminated throughout the matrix. Microscopic veinlets of quartz cutting across the original layering are also observed (e.g., Figure 3a).

4.1.2 | Microscopic Observations

Microscopically, FD55-463.50 and FD55-384.43 consist of a mm-scale layering composed of relatively coarse (> 100 μm in size) sub- to euhedral magnetite grains (dark metallic layers in Figure 2a,b), alternating with domain composed of a fine layering of white chert and microcrystalline hematite. In these finely layered domains, magnetite of different sizes (from 1 to 100 μm dimension) occur either as randomly distributed "hotspots" or define a vague orientation parallel to layering (Figure S1). SEM images show that the microcrystalline hematite layers are either homogeneous (Figure 2c,e,f) or contain variable amounts of randomly distributed 10–20 μm large spherule-like features composed of microcrystalline quartz (Figure 2d,g; see also Figures 4 and 5). The abbreviations and nomenclature for the different generations of hematite described are summarized in Table 1. In some samples, the abundance of Si-spherules is so high that it forms a mosaic of spots mimicking a "honeycomb structure" (Figures 2d and 5a,c). In both types of layers, hematite occurs as a dense network of randomly distributed and intertwined, μm-scale hematite grains (H1m, Figure 4). The internal structure of Si-spherules is homogeneous or locally shows the occurrence of well-individualized nano- to microscopic hematite localized in the cores, lining the outer rims of the Si-spherules, or both (Figure 4a–d). Detailed microscopic investigations allowed identifying two types of hematite inclusions within Si-spherules. H1s inclusions are present only in the best-preserved sample FD55-463.50 (Figure 4a). There, hematite inclusions form a random network of ~100 to 200 nm large hematite grains throughout the Si-spherules (H1s). Another type corresponds to a population of slightly bigger grains (~500 nm in size) located in the core of the Si-spherules [H1s(re) in Figure 4b]. These nm-scale inclusions H1s and H1s(re) are different from the μm-scale matrix hematite H1m. Type 2 hematite inclusions are by far the most common (Figures 4d and 5). These inclusions show the same size as the surrounding matrix hematite (~1 μm in size) and occur exclusively along the margins of the Si-spherules. The thickness of these hematite rims varies greatly from one Si-spherule to another (Figure 5d,e) and within the same spherule (Figure 4d). This change in the size of hematite inclusion rims seems to increase to ultimately form a matrix composed of randomly distributed matrix hematite grains embedded in quartz (Figure 5f). In these domains, the dense hematite matrix (H1m) occurs as small isolated islands in a matrix composed of dispersed hematite and chert. Figures 3d and 5h show that, in some samples, the original H1m grains are no longer preserved and the matrix appears mainly composed of quartz and diffuse hematite grains [hematite dust, according to Lindenmayer, Laux, and Teixeira 2001, and also described as post-depositional dehydration or oxidation products by Sun et al. (2015) and Rasmussen et al. (2016)] of unknown generation (Hn) that discreetly emphasize the rounded shape of the original Si-spherules.

Magnetite is present in all types of layers. It occurs as euhedral to subhedral grains of variable sizes overprinting the original layering. The internal structure of most magnetite varies as a function of the nature of the underlying matrix. When the host matrix is composed of microcrystalline matrix hematite (H1m), magnetite occurs as euhedral, inclusion-free blasts overprinting the matrix (Figure 2e). If magnetite overlaps alternate chert and jasper layers, the original layering occurs preserved in magnetite as indicated by the occurrence of microcrystalline quartz inclusions in the magnetite domains overlapping the cherty layer and absence in the domains overlapping the hematite layers (Figure 2f). If Si-spherules are present in the

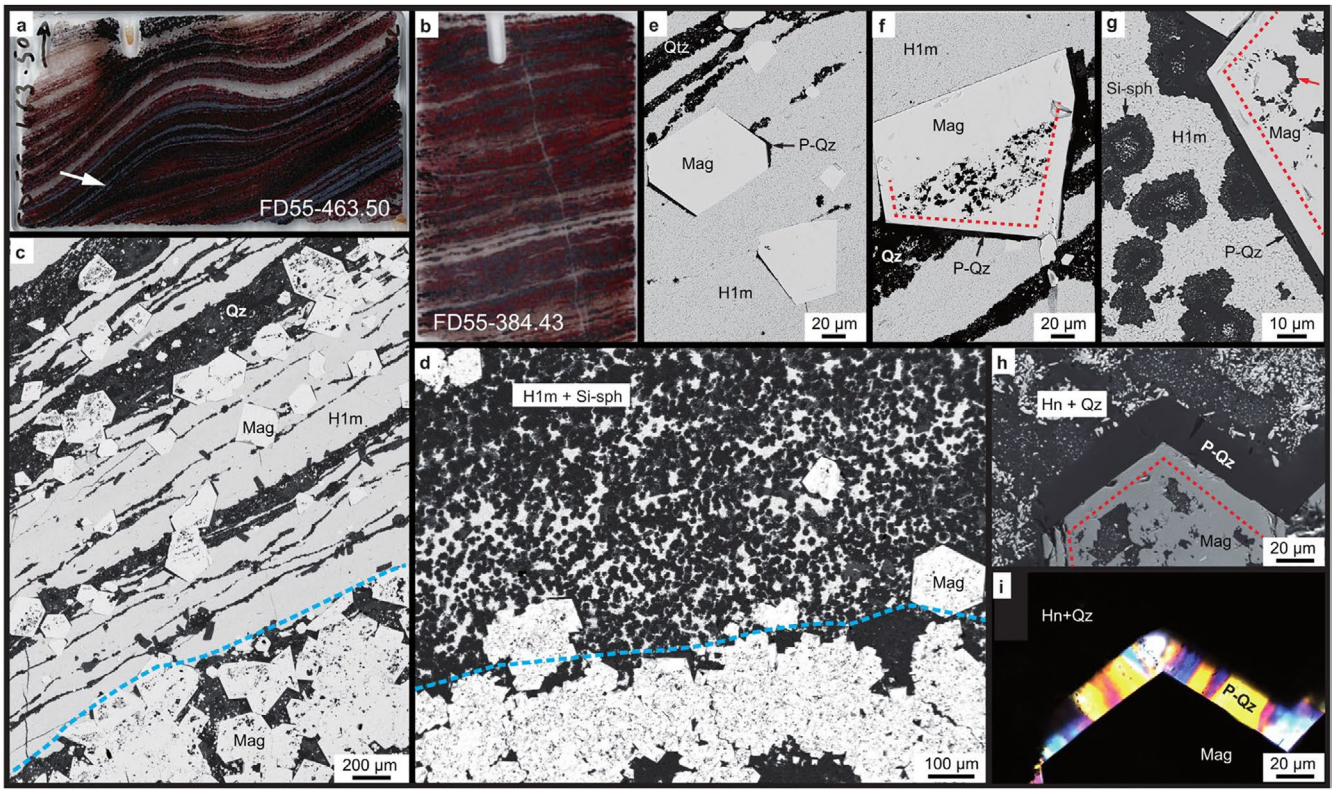

FIGURE 2 | (a, b) Petrographic thin sections (2.6×4.6 cm) of samples FD55-463.50 and FD55-384.40 characterized by finely laminated BIFs displaying horizontal to wavy lamination and erosional surface (arrowed). Stratigraphic top is indicated by a diamond saw incision. (c, d) Low magnification images of the microstructures present in samples FD55-463.50 (c) and FD55-384.40 (d). Blue dashed lines separate a magnetite-rich layer at the base [dark metallic layers in (a, b) from a jasper domain above (reddish layers)]. (c) Alternate layers of microcrystalline matrix hematite H1m and quartz, magnetite (Mag), and white chert (Qz). (e, f) Detail of (c) showing (e) two inclusion-free magnetite blasts overprinting a H1m-rich layer and (f) a magnetite blast formed above a layered structure composed of white chert (Qz) and matrix hematite (H1m). Note the occurrence of quartz inclusions mimicking the trace of the underlying chert layer and absence in the magnetite zone formed over the H1m layer. The red dashed line underlines an inclusion-free magnetite rim. P–Qz (arrowed) points to a thin layer of palisade quartz developing as pressure solution along the magnetite crystallographic faces oriented perpendicular to the layering. (d, g) SEM images of sample FD55-384.43 showing the "honeycomb structure" composed of Si-spherules disseminated in matrix hematite H1m (d) and closer view of the contact between a magnetite blast overprinting the H1m + Si-sph matrix (g). Note the occurrence of several generations of misoriented microscopic hematite inclusions in the core and rim of the Si-spherules (see Figure 4d,f). The red arrow in magnetite points to a rounded quartz structure mimicking the underlying Si-spherule shape. The dashed line underlines an inclusion-free overgrowth zones in magnetite. Note the truncation of the matrix Si-spherule by the magnetite overgrowth zone and the secondary superposition of a thin fringe of palisade quartz (P-Qz) separating the truncated Si-spherule from the magnetite overgrowth zone. (h, i) SEM (h) and optical microscope (i) images of a palisade quartz (P-Qz) separating a magnetite grain (Mag) from a matrix composed of hematite of unknown generation (Hn) and quartz (see text). Note the radial character of quartz grains oriented perpendicular to the magnetite crystallographic faces (i).

host matrix, magnetite can preserve the ghost shape of the overgrown spherules (Figures 2g, 3c, and 5b,c). Importantly, the inclusion-rich zones mimicking the trace of the underlying cherty layers or Si-spherules occur generally truncated near the magnetite rims (Figures 2f–h, 3c,f, and 5b). This truncation can be observed as a distinct feature of a second stage of magnetite growth. These overgrowth zones are present in the vast majority of samples, independently of the degree of diagenetic/metamorphic re-equilibration (e.g., Figure 3c,f). Contrary to magnetite cores, the overgrowth zones are inclusion free and develop independently of the nature of the underlying matrix. In samples FD55-463.50 and FD55-384.43, high-resolution imaging of the contact between magnetite and matrix hematite reveals the occurrence margin-parallel, ultrathin layers (nm-scale) of indistinguishable oxides along magnetite crystallographic faces (Figure 4e,f). Importantly, note that the thickness of the overgrowth zones is bigger in magnetite–quartz layers than in the ferruginous chert (compare Figure 3c,f with Figure 5b). A final texture concerns the occurrence of magnetite blasts consisting of a mosaic of darker and lighter subdomains (Figure 3g,h). These internal structures are found in sample FD55-349.06, which is composed of magnetite and quartz with minor residual hematite.

Regarding the silica-rich structures, in contrast to the spherule-like features described above, amalgamated Si-spherules (Figure 5c,e,g) were also observed under SEM. These spherules tend to lose their rounded shape to ultimately define a quartz-rich area with vague preservation of the original honeycomb texture (Figures 2d and 5h). Additionally, Si was also found as palisade-quartz (P-Qz; Figures 2 and 3) forming a columnar structure radiating out perpendicular to large magnetite grain surfaces and delineating a sharp contact between magnetite and the surrounding matrix (Figure 2i). Note that the palisade quartz oriented normal to the layering

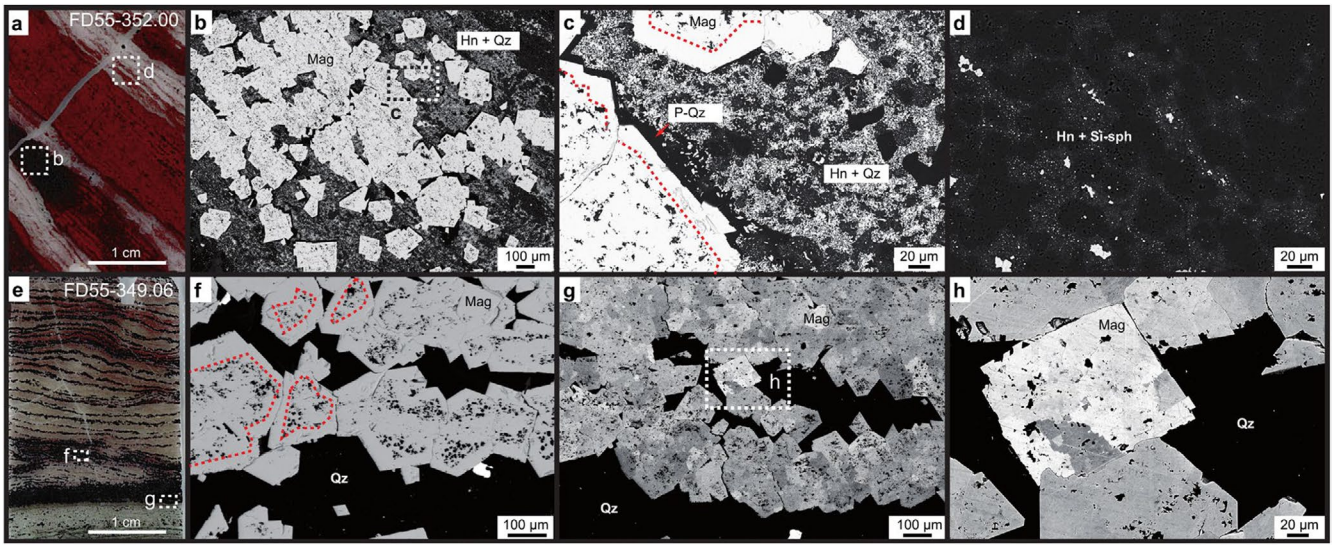

FIGURE 3 | (a–d) Petrographic thin section (2.6×4.6 cm) of sample FD55-352.00 showing mesobands of reddish jaspilitic BIF evolving laterally either into lighter domains composed of white chert (d) or darker domain (b, c) enriched in large (200–500 µm) magnetite grains (Mag). (c) Close-up view of (b) showing magnetite blasts overprinting a matrix composed of matrix hematite of unknown generation (Hn) and microcrystalline quartz (Qz). The red dashed line highlights magnetite overgrowth zones. P-Qz is for palisade-quartz. (e) Petrographic thin section (2.6×4.6 cm) of sample FD55-349.06 showing the predominance of white chert and magnetite layers. (f) Magnetite grains showing large, inclusion-free overgrowth zones (red dashed lines). (g, h) Internal structure of magnetite grains characterized by a mosaic of darker and lighter domains attributed to local changes in the composition (Si–Fe solution) and/or crystallographic orientation within individual magnetite crystal (see text).

(pressure shadow) also occurs in continuity with the magnetite overgrowth zones.

4.2 | Magnetic Parameters

After removing the paramagnetic contribution, most samples from the Carajás section exhibited uniform and well-defined hysteresis loops, characterized by low coercivity (H_c) and high-saturation magnetization M_s, typical of large multi-domain (MD) magnetite grains (Dunlop and Özdemir 1997), see Figure S2. The presence of hematite is not readily discernible and is masked by the substantial abundance of magnetite. This is due to the fact that magnetite saturation magnetization (~92 Am^2/kg) is significantly higher than that of hematite (~0.5 Am^2/kg) (O'Reilly 1984). The hysteresis parameters extracted from the hysteresis loops are reported in Table S1; M_s and M_{rs}/M_s are plotted as a function of depth along with the stratigraphy (when subsamples are located at less than 1 cm depth distance the mean value is plotted) (Figure 6b,c). Over the entire section, the averaged M_s is 25 Am^2/kg. The lowest measured values are around 5–6 Am^2/kg and are found at around 479.4 and 515.2 m depth, which corresponds to the Fe-poor carbonate interval. Variations in M_s values within the sections are commonly attributed to changes in magnetite content. Therefore, as a first approximation, the mass percentage of magnetite in a sample can be estimated using Equation (2):

$$\mathrm{Mt}_{\mathrm{wt\%}} = \frac{M_s \times 100}{92} \quad (2)$$

where an M_s value of 92 Am^2/kg corresponds to pure magnetite.

The M_s data are compared to the percentage of magnetite obtained for 15 samples through X-ray diffraction (XRD) refinement by the Rietveld method and show very good agreement. The M_{rs}/M_s ratio is indicative of the grain size. According to the diagram proposed by Day, Fuller, and Schmidt (1977) and the theoretical mixing curves of Dunlop (2002) (not shown), values of $M_{rs}/M_s \leq 0.1$ are typical of assemblages of multi-domain (MD) magnetite associated with coarse magnetite grains (see also Dunlop and Özdemir 1997). In Figure 6c, we observe that the BIFs interval exhibits an average M_{rs}/M_s of 0.07, attesting for the large size of the magnetic domain, with few exceptions, such as around the depth of ~350 m, and next to the carbonate layers which shows relatively higher M_{rs}/M_s values (0.15), reflecting the contribution of magnetite populations with smaller grain sizes in these layers.

Isothermal remanent magnetizations acquisition curves are commonly used to improve the characterization of the magnetic carriers by bringing to light the spectrum of coercive forces and would be particularly useful in our case where the two main magnetic minerals (magnetite and hematite) have contrasting coercivity (e.g., Kruiver et al. 2003). However, it is notably difficult to identify hematite when it is mixed together with magnetite, because of the high saturation magnetization of magnetite compared to hematite (e.g., Liu et al. 2019). Nevertheless, the high-field parameter (HIRM) has proven effective in detecting medium to low concentrations of hematite mixed with magnetite (Liu et al. 2019). Additionally, the magnitude of the HIRM offers the advantage of reflecting the concentration of hematite (Frank and Nowaczyk 2008).

Figure S3a presents an example of IRM measurements for a synthetic sample containing equal proportions of hematite and magnetite. Typical examples of IRM acquisition curves are shown in Figure S3b–d for samples FD55-463.50, FD55-352.00, FD55-349.06, corresponding to observed thin sections in Figures 2a and 3a,e. All IRM curves exhibit a sharp increase for

fields lower than 0.1 T, confirming the predominance of magnetite in the magnetic signal. Most samples approach saturation at fields as low as ~0.2 T (sometimes 0.1 T), and in the majority of cases (though not universally), there is a slight increase in magnetization observed, especially after 0.2 T, up to the maximum field of 1 T, indicating the presence of hematite. Most samples show a very moderate increase in magnetization, as depicted in Figure S3c,d, and clear instances occur, such as in sample FD55-426.07 in Figure S3e, but are far from being the norm. For a few samples, a small decrease is observed after 0.5 T (Figure S3b). This phenomenon could be associated with the presence of large multidomain magnetite grains, which are typically less stable. The combination of small relaxation time and low coercivity add a bias to the remanence measurements during high-field experiments, possibly due to the small back field induced during the experiments. Changes of experimental conditions did not improve the results to sufficient quality. We observed that this bias could be suspected to happen above 0.8 T in many samples. Owing to their large size, magnetite grains have low coercivities and it is reasonable to consider that they are fully saturated by 0.2 T. In contrast, high remanent coercivity is observed in pseudocubic hematite grains with sizes ranging from 0.5 to 2 μm (e.g., Dekkers and Linssen 1989; Kletetschka and Wasilewski 2002; Liu et al. 2010), a characteristic that aligns with a significant part of the hematite population observed in the samples. With this consideration and experimental caveats discussed above, HIRM was calculated to estimate the concentration of hematite but the formula used here has been slightly modified to minimize the bias due to large MD magnetite that appears typically after 0.8 T. Specifically, we used Equation (3) instead of Equation (4) as follows:

$$\mathrm{HIRM} = \frac{M_{0.8T} - M_{-0.2T}}{2} \tag{3}$$

$$\mathrm{HIRM} = \frac{M_{1T} - M_{-0.3T}}{2} \tag{4}$$

By doing so we excluded the large MD magnetite grains but kept most of the hematite signal. The calculated HIRM represents the relative abundance of hematite. This relative abundance can be directly converted into absolute concentration using a multiplicative factor that depends, to a limited extent, on the average hematite crystal size. In our case, the observed hematite population consists of nano-hematite with similar characteristics throughout the depth interval, suggesting that this relative abundance is indeed proportional to concentration, with a consistent proportional factor throughout the section. The results are presented in Figure 6d as HIRM* (HIRM normalized to magnetite). The Hm/Mt ratio obtained through Rietveld method X-ray diffraction (XRD) is presented to establish a comparative analysis of variations in hematite concentrations with those obtained from magnetic measurements. Similar trends are observed, reinforcing confidence in the dataset (Figure 6d). Notably, an HIRM* value of 0.2 corresponds to a concentration of approximately equal proportions of hematite and magnetite (see also Figure S3a).

The HIRM* data show significant variations along the section, featuring low values in intervals around 340–380, 480 m, and at depths beyond 512 m. In contrast, depth intervals between 300–330, 400–450, and 475–500 m show higher values. S-ratio is another widely used parameter to estimate the proportion of high coercivity minerals. It was calculated here using a saturation field of 800 mT and a back-field of −200 mT (Equation 5):

$$S-\mathrm{ratio}^{*} = \frac{1}{2}\left(\frac{M_{0.8T} - M_{-0.2T}}{M_{0.8T}}\right) \tag{5}$$

Modified from Bloemendal et al. (1992) (Table S1). The results indicate S-ratio* values ranging between 1 and 0.96, suggesting the predominance of low-coercivity phases, with a minor contribution from high-coercivity phases, as evidenced by values deviating slightly from 1 toward smaller values. As expected, S-ratio* variations are anticorrelated with HIRM*.

Low-temperature susceptibility curves performed on 32 powdered bulk samples are characterized by a transition in the magnetic susceptibility at around ~100–120 K for all samples, which is characteristic of the Verwey transition (T_V) of magnetite. By plotting the first derivative of magnetic susceptibility against temperature, three distinct behaviors were observed (see Figure 7). The least common pattern exhibited a smoothed transition with a derivative peak typically occurring around 100–110 K, exemplified by samples FD55-349.06 and FD55-476.765 (as shown in Figure 7a,d). A second pattern comprised samples displaying a double Verwey transition, such as sample FD55-463.58 (depicted in Figure 7c), characterized by a prominent sharp peak around 120 K and a secondary peak around 100 K. Most samples belong to a last group characterized by a single peak with maximum intensity at approximately 120 K (e.g., sample FD55-352.05, as illustrated in Figure 7b).

The Verwey transition estimates presented above are derived from the susceptibility curves, which have the advantage of being relatively easy to produce, but Verwey transition can also be derived from remanence magnetization curves using an MPMS. In order to check for consistency, four samples were also subjected to MPMS measurements, and almost identical T_V values and behavior were found (Figure S4). We note that the ZFC derivatives exhibit slightly narrower peaks compared to the susceptibility derivative. We further note that ZFC curves consistently exhibit higher values than field-cooled (FC) curves (Figure S5). This, coupled with relatively low-temperature (R_{LT}) values ranging between 0.61 and 0.83, suggests the prevalence of multi-domain magnetite (Smirnov 2009).

Lastly, high-temperature magnetic susceptibility experiments were acquired. The BIF and Fe-carbonate samples show a very homogeneous behavior, with all curves displaying one marked transition at ~580°C, which corresponds to the Curie temperature of magnetite (Figure S6). In some cases (e.g., FD55-463.50 and FD55-514.70), a faint signal remains above 580°C, which corresponds to contributions of hematite.

5 | Discussion

The integration of detailed petrographic observations and magnetic data has allowed us to identify various stages of iron oxide crystallization in Carajás BIFs. First, we discuss the most

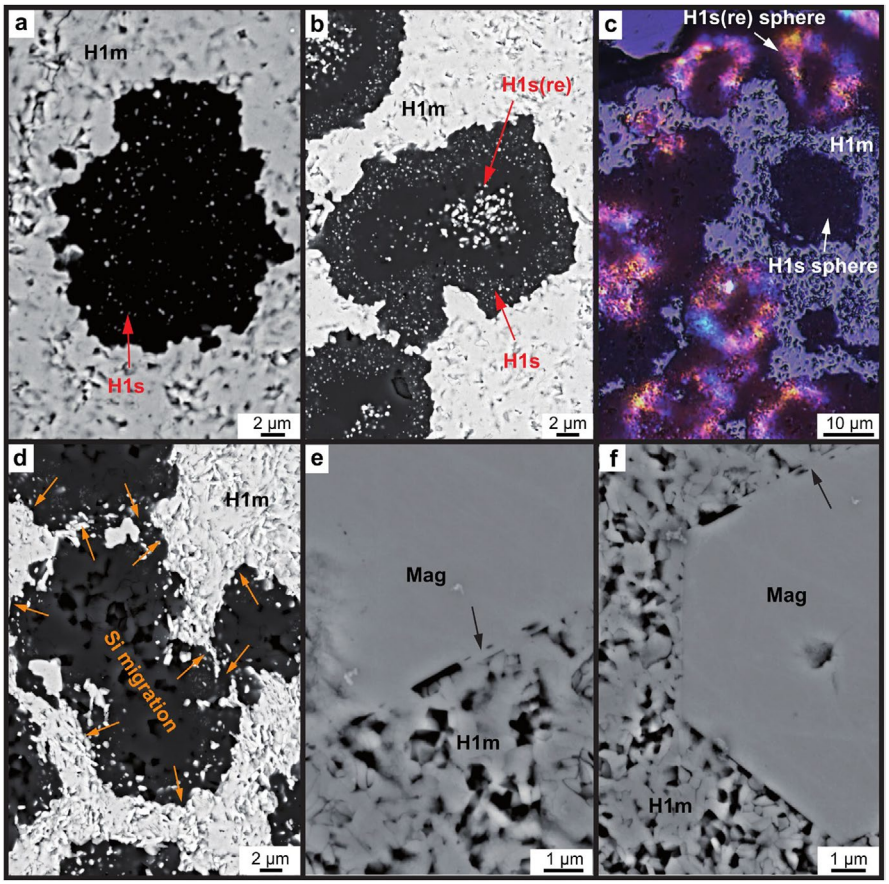

FIGURE 4 | (a–d) Si-spherules internal structure (sample FD55-463.50). (a) H1s, primary ~100 nm-scale hematite inclusions in Si-spherule. (b) H1s(re), primary ~500 nm-scale hematite inclusions located in Si-spherule cores interpreted to have formed after H1s inclusions. (c) Polarized/transmitted light microscope photograph showing primary dark Si-spherules composed of misoriented quartz and hosting H1s hematite inclusions and more evolved Si-spherules displaying spheric haloes of radial quartz (palisade quartz) and containing H1s(re) in their core. (d) Apparent µm-scale hematite inclusions lining Si-spherule rims attributed to matrix hematite H1m isolated from the margin as a consequence of silica migration (illustrated with orange arrows, see text and Figure 5). (e, f) SEM images of the contact between magnetite blast (Mag) and matrix hematite (H1m) [samples FD55-384.40 (e) and FD55-463.50 (f)]. Note the margin-parallel ultra-thin layers (arrowed) oriented parallel to magnetite crystallographic faces interpreted to reflect the mode of magnetite overgrowth via thermochemical Fe(III) reduction.

common assumptions found in the literature regarding which minerals and features are considered primary precipitates in Precambrian BIFs. We then examine whether the presence of the microcrystalline hematite–quartz assemblage, characterized by a honeycomb structure consisting of well-crystallized Si-spherules randomly dispersed within the hematite matrix, can be considered evidence for the sedimentary origin of the Carajás BIFs. Second, we discuss the possible crystallization pathways of hematite and magnetite, the variations in the magnetic signal along the stratigraphy and their implications for the rock record. The specific properties of carbonate-rich intervals which precipitates in shallow and more reduced environment (Rego et al. 2021; Rossignol et al. 2023) are briefly discussed. Finally, by combining the characterization of petrographic observations and magnetic properties with Fe isotope data obtained in the same samples (Rego et al. 2021), we propose a plausible scenario for the prevailing paleoenvironmental conditions during the deposition of the Carajás BIFs. It is worth emphasizing that the stratigraphic successions deposited in the Carajás Basin experienced only low greenschist facies metamorphic conditions (Macambira 2003; Martins et al. 2022). Our petrographic observations further support the minimal impact of post-depositional processes on the studied samples.

5.1 | Primary Precipitates

The nature of the original precipitates in BIFs, even in the best-preserved samples, has long been a topic of significant discussion. This stems partly from the immense challenge of accurately reconstructing the environmental conditions under which they were formed, and from the wide range of diagenetic and metamorphic processes to which these chemical sedimentary rocks may have been exposed since the Precambrian. In the case of our Carajás BIFs samples, high HIRM* values measured along the studied drill core indicate a high concentration of hematite in almost all non-carbonate intervals. SEM observations reveal that hematite predominantly occurs as fine grains forming honeycomb-like aggregates (Figures 2d,g and 5a,b). Such clusters of Si-rich microgranules associated with hematite nanoparticles have been previously documented in the literature and linked to primary and possibly biological structures (Lindenmayer, Laux, and Teixeira 2001; Ribeiro da Luz and Crowley 2012). In contrast, other studies proposed that similar hematite structures in BIFs originated from the fluid-mediated replacement of iron silicates and iron carbonates (e.g., Dales Gorge Member, Rasmussen, Krapež, and Meier 2014). The presence of Si-spherules with nano-scale H1s inclusions, embedded

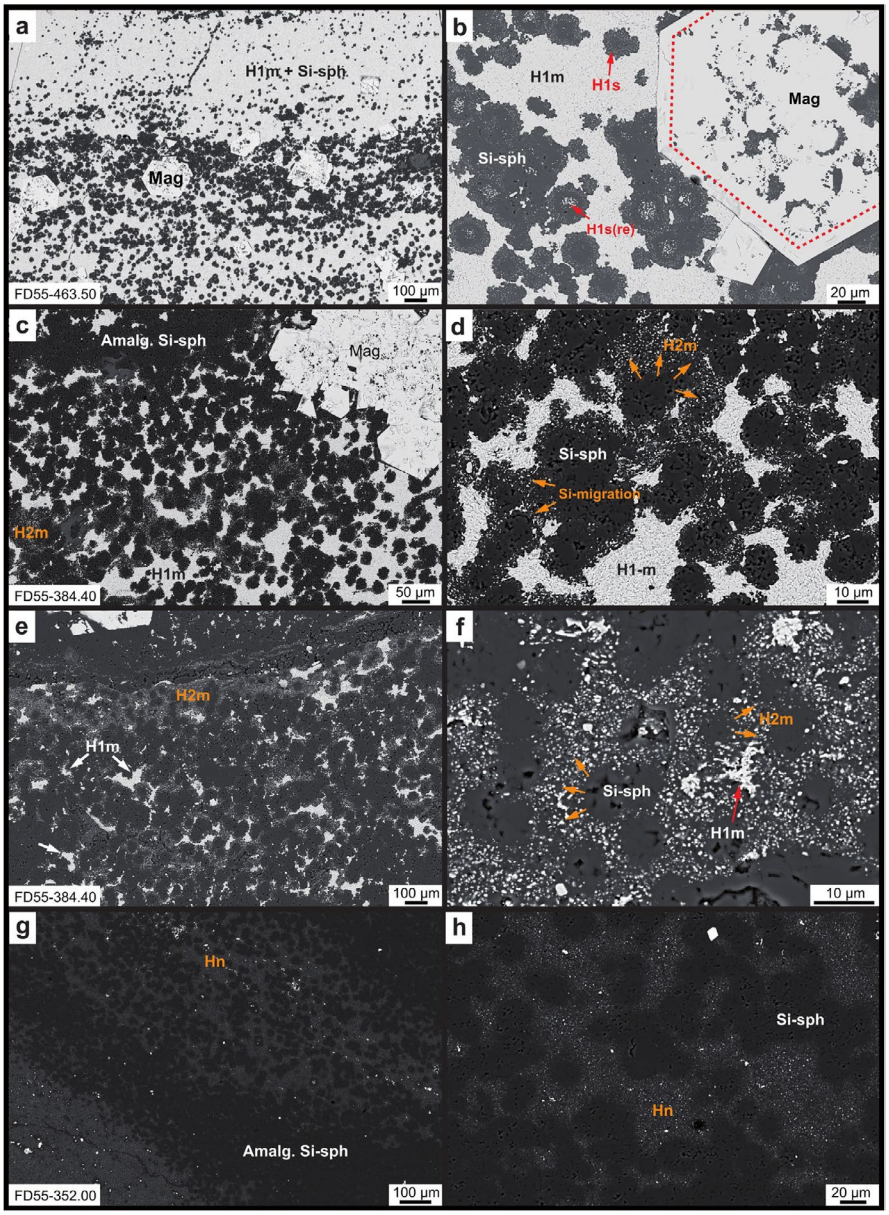

FIGURE 5 | Evolution of the composition and texture of jasper layers with increasing diagenetic alteration. (a, b) "Honeycomb" texture preserving primary matrix hematite H1m, Si-spherule (Si-sph), and hematite inclusions H1s and H1s(re). Dashed line in (b) underlines an inclusion-free overgrowth zone in magnetite (Mag). (c, d) Increasing silica content leading to disruption and local amalgamation of Si-spherules (Amalg. Si-sph). Primary hematite H1m largely preserved but locally dispersed in quartz-enriched domains to form H2m. (e, f) Advanced stage of diagenetic alteration where the honeycomb structure appears strongly modified due to increase silica impregnation (illustrated with orange arrows). Original matrix hematite H1m only locally preserved. (g, h) Extreme stage of alteration characterized by a matrix composed of quartz and diffuse hematite grains of unknown generation (Hn) that discreetly emphasize the rounded shape of the original Si-spherules.

TABLE 1 | Summary of hematite generations: Abbreviations and morphological differences.

Abbreviation	Generation	Description
H1s	Primary inclusions	Nanometer scale hematite inclusions
H1s(re)	Early secondary inclusions	Recrystallized H1s grains
H1m	Primary matrix hematite	Micrometer scale hematite grains composing the original hematitic matrix
H2m	Secondary	H1m grains dispersed in Si-rich domains
Hn	Unknown	Residual hematite grains in chert

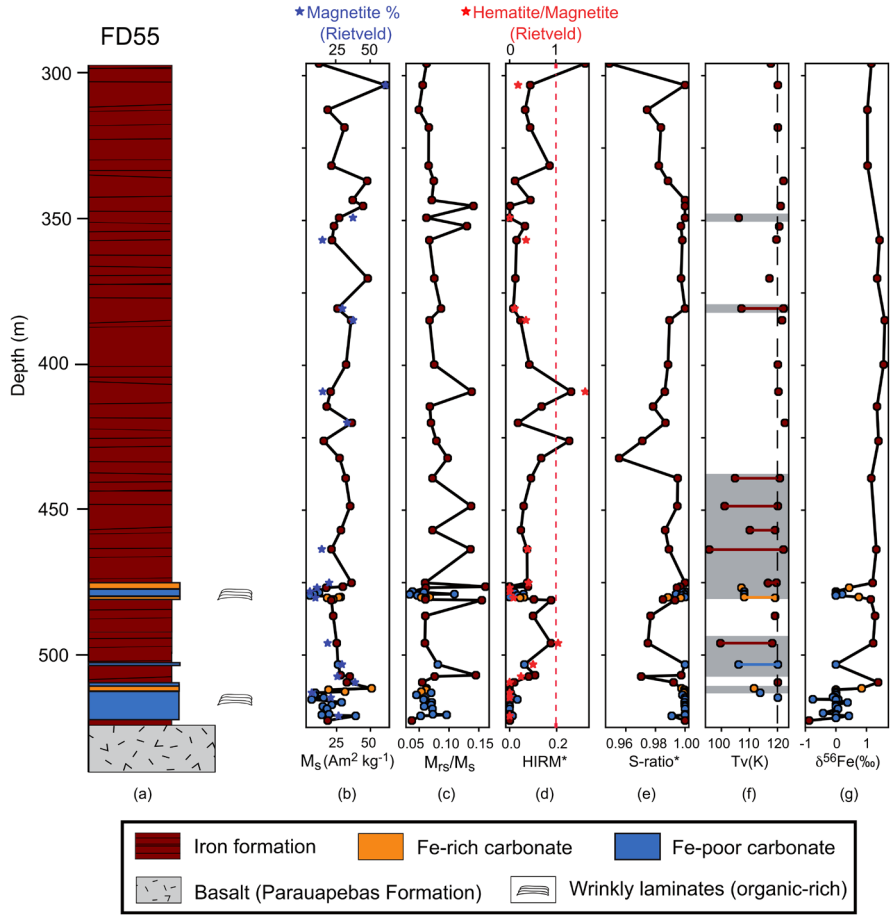

FIGURE 6 | Magnetic parameters, XRD results, and Fe isotope as a function of depth, the color code of data point is following the lithology. (a) Stratigraphic log of core FD55 after Rego et al. (2021) and Rossignol et al. (2023). (b) Saturation magnetization (M_s) used as a proxy for the amount of magnetite [Mt (in Wt%) $\simeq 1.09 \times M_s$]; blue stars represent magnetite in phase % according to the Rietveld method. (c) M_{rs}/M_s values, a proxy for magnetite grain sizes, with lower values associated with larger grains. (d) Hard isothermal remanent magnetization (HIRM*%), defined as {[0.5 × S IRM(800) + IRM(−200 mT)] × (100/M_s)}, used as a proxy for hematite relative to magnetite; red stars represent hematite in phase % according to the Rietveld method. The dashed red line marks the values above which hematite dominates over magnetite (i.e., Hm/Mt. ratio greater than 1), note that it corresponds to values of HIRM* above 0.2. (e) S-ratio* calculated from Bloemendal et al. (1992) used as a proxy for the relative abundance variations of hematite and magnetite; an S-ratio of 1 is representative of a sample with only magnetite, the larger the departure from this value the higher the contribution of hematite. (f) Temperature (in K) of Verwey transition of magnetite; values below 120 K are interpreted as non-stoichiometric magnetite and are highlighted in gray. (g) Fe-isotope composition from Rego et al. (2021) showing a consistent and narrow positive range in δ^{56}Fe values for the BIFs interval.

in misoriented microquartz within the hematite rich zone, suggests they represent remnants of a primitive assemblage comprising ferrihydrite particles and aqueous silica (Figure 4a,c). The nearly spherical morphology of these spherules suggests they formed in the water column or during the very early stages of sedimentation in a water-saturated and unconsolidated environment. The absence of microquartz orientation and the random and homogeneous distribution of H1s inclusions within individual spherules support an nm-scale for the primary ferrihydrite and rapid replacement by nm-scale hematite pseudomorphs as similarly proposed for other Neoarchean IFs (e.g., Weld Range, Czaja et al. 2018). This suggests that the replacement of ferrihydrite into nano-scale hematite occurred with very limited element mobility, which is typically the scale of a crystallization process dominated by Ostwald ripening (Sun et al. 2015). The occurrence of spherules containing radial microcrystalline quartz devoid of hematite inclusions and defining spherical haloes around a central core preserving micro-scale H1s(re) inclusions (Figure 4b,c) argues for a stage of silica remobilization and Fe-oxide recrystallization on a μm-scale. Moreover, at the scale of our observations, no Fe-silicate minerals such as greenalite associated with dusty hematite were found in the studied samples (Rasmussen, Krapež, and Meier 2014; Rasmussen, Muhling, and Krapež 2021). The absence of Fe silicates could arise from a bias in sample preservation and/or be due to alternative pathways for hematite formation.

5.2 | Magnetite Formation

Studies investigating the paragenesis of BIFs invoke various scenarios to explain the relationship between hematite formation and other commonly observed Fe-oxides such as magnetite (Konhauser et al. 2017). According to Klein (2005), ultrafine magnetite particles may result from the dehydration of primary iron oxyhydroxide precipitates. Alternatively, Li et al. (2013)

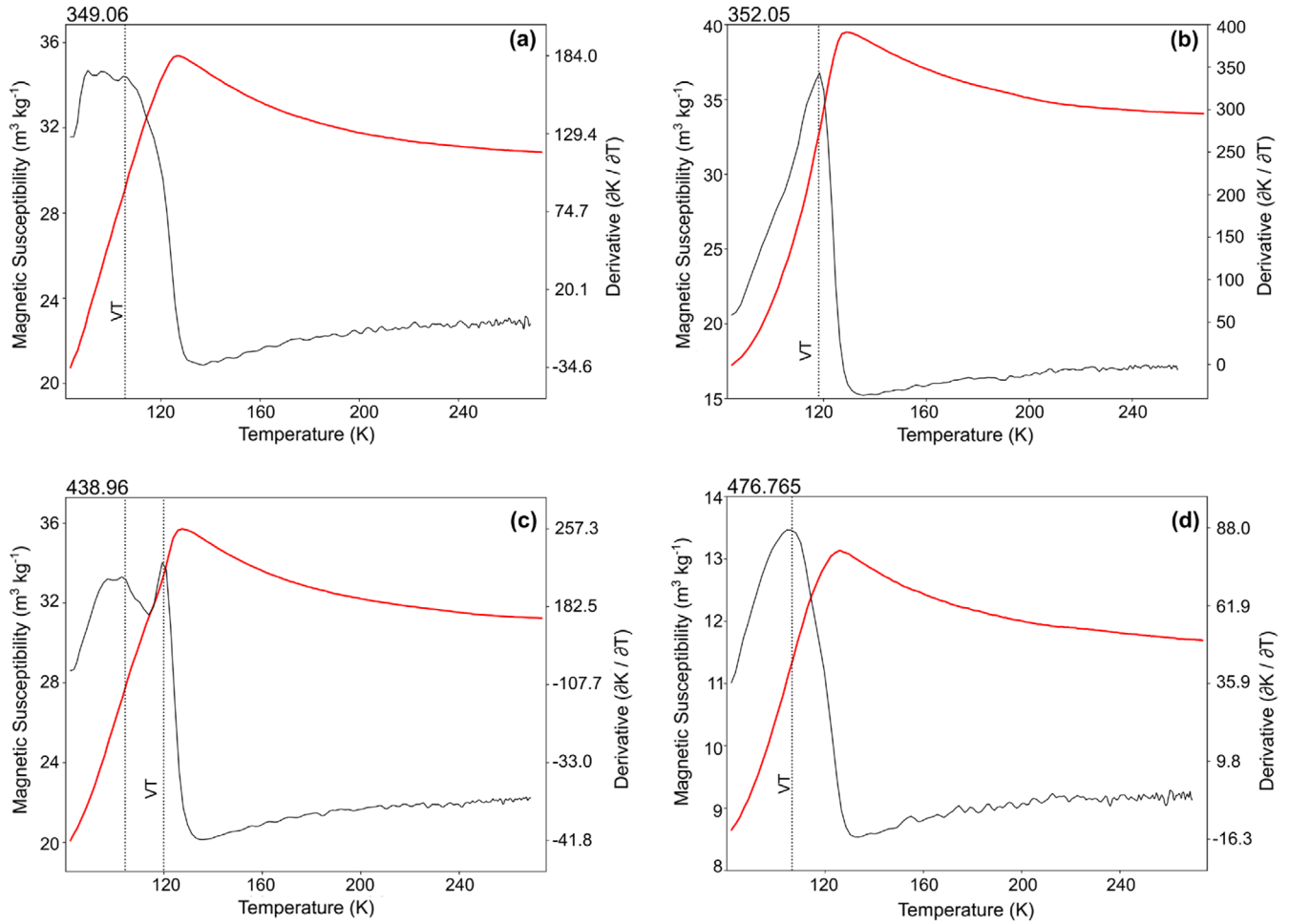

FIGURE 7 | Mass-normalized magnetic susceptibility curves (in red) and their first derivatives versus temperature (in black) of bulk samples from drill core FD55. Representative samples show: (a) The large amplitude of the first derivative curve indicates that the Verwey transition (VT) spans a temperature range between 90°C and 120°C; (b) single VT representing the stoichiometric purity of magnetite observed when the Verwey transition peak occurs at 120 K; (c) the presence of two peaks in this sample corresponds to 2VT, one occurring at approximately 104 K and another with a peak closer to 120 K; (d) A single VT peak near 120 K. Higher amplitude of the peak also indicates that there is some factor affecting the stoichiometric behavior of magnetite. Note that the different panels have different scales on the Y-axis.

have presented experimental evidence supporting the formation of magnetite through the biological-mediated dissolution of poorly crystalline iron oxyhydroxides (e.g., ferrihydrite), while other studies favored magnetite formation in late stages associated with metamorphic and deformation processes (Van Zuilen et al. 2003; Rasmussen, Muhling, and Krapež 2021). High values of M_s and the occurrence of magnetite as euhedral grains of very different sizes embedded or overprinting the primary hematite–silica layering and honeycomb structure in BIFs from Carajás (See Figure S1) clearly support that magnetite formed during or soon after the microcrystalline hematite–quartz matrix. The preservation of microquartz primary textures as "ghosts" within magnetite cores (Figure 2g) indicates that nucleation of a magnetite precursor in the water column using hydrothermal Fe(II) is not an option. Another argument against the possibility of magnetite originating from pelagic sediments is the absence of framboidal magnetite in our samples, which according to Vuillemin et al. (2023) would indicate their precipitation from the water column in Earth's early oceans. These observations suggest that magnetite formation in Carajás likely occurred as a result of a reductive process as similarly observed in other BIFs (e.g., Cauê Iron Formation, Teixeira et al. 2017).

The occurrence of microcrystalline magnetite embedded in the hematite–quartz matrix in some of the well-preserved samples such as FD-55-384.43 and FD55-463.50 (Figure S1), suggests that magnetite could have formed early and could be synchronous with hematite crystallization after ferrihydrite as supported by the preservation of spherule "ghosts" in the larger magnetite grains. Therefore, a well-established and plausible mechanism for the reduction of ferrihydrite and/or hematite to magnetite in a water-saturated and unconsolidated sediment prior to lithification is DIR. Microbial DIR is an anaerobic respiration metabolism in which ferric iron is an electron acceptor and organic C and H_2 are electron donors (Lovley and Ohillips 1986; Lovley et al. 1987). This iron reduction mechanism is often used to explain the accumulation of Fe-oxides and Fe-rich carbonates (e.g., magnetite and siderite) in BIFs (Johnson et al. 2005; Konhauser, Newman, and Kappler 2005; Heimann et al. 2010; Craddock and Dauphas 2011; Li et al. 2013; Smith, Beukes, and Gutzmer 2013; Teixeira et al. 2017; Smith and Beukes 2023). Based on the textural relationships described above, this reducing process most likely involved a diffusion-controlled mechanism under limiting Fe(II) availability. This leads us to discard models of magnetite formation that invoke

the percolation of Fe(II)-rich fluids, such as that proposed by Czaja et al. (2018).

In contrast, the magnetite rims devoid of mineral inclusions and the occasional absence of spherule "ghosts" support a different crystallization process. Large magnetite overgrowth zones are found in layers that exhibit clear signs of pervasive silicification of the rock matrix likely reflecting a more evolved stage of diagenesis and/or low-grade metamorphism. As shown in Figure 4e,f, the occurrence of nano-scale Fe-oxide layers lining the contact between matrix microcrystalline hematite and inclusion-free magnetite strongly suggests that magnetite overgrowth zones could have formed after hematite. Hence, a plausible scenario for the formation of magnetite overgrowth zones during late diagenesis, low-grade metamorphism, is thermochemical Fe(III) reduction of matrix hematite (Köhler et al. 2013; Posth et al. 2013; Halama et al. 2016). Interestingly, the occurrence of two Verwey transitions in some samples (e.g., FD55-438.96) may be indicative of the detection of these two types of magnetite (cores and rims), as differences in Verwey temperatures is commonly used as an indicator of the degree of magnetite purity (Jackson and Moskowitz 2021). To our knowledge, this pattern of inclusion-rich cores and inclusion-free rims had not been described previously. In strongly silicified samples in which hematite is only a residual phase (e.g., sample at 349.60 m depth), as also evidenced by the low HIRM* values, magnetite grains occur as large blasts composed of different sub-domains which exhibit zonation patterns, evidenced by bright and dark domains (Figure 3g,h). Interestingly, the magnetic properties display smoothed Verwey transition curves in these layers. These features might be associated with local changes in the composition (e.g., Si content) and/or distinct crystallographic orientations within individual magnetite crystals. This suggests that these magnetite populations likely underwent some form of alteration.

Lastly, the carbonate-rich intervals are characterized by low hematite and magnetite concentrations relative to the rest of the section and soft Verwey transitions with initiation well below the Verwey reference temperature of 120 K (i.e., ranging from 107.15 to 113.85 K). In these horizons, magnetite exhibits a large range of non-stoichiometry degree. These variations may be attributed to partial substitution by elements such as Si and/or light elements which remained undetected in the EDSX analyses or an unbalanced ratio between Fe(II) and Fe(III) (Chang et al. 2015). The inferred depositional settings for these layers are discussed in Rossignol et al. (2023), who suggest shallow water depth and possible high organic carbon production. We infer that the magnetite associated with such depositional processes are non-stoichiometric. The correlation between the crystal structure of magnetite and Archean microbial activity within these particular carbonate layers remains to be explored in more detail.

5.3 | Significance of Fe Isotopic Data

The Fe isotope compositions of BIFs reported by Rego et al. (2021) show remarkably homogeneous and positive δ^{56}Fe values between +1.03 and +1.95‰ (average of +1.39 ± 0.22‰) throughout the studied drill core. This positive and homogeneous Fe isotopic signal coupled with ^{13}C-depleted organic matter have been attributed to the activity of photoferrotrophs. These microorganisms are commonly associated with the generation of Fe(III) in Archean BIFs (Konhauser et al. 2002). The magnetic properties found in this study on the same samples exhibit notable fluctuations in the hematite ratio parameter (HIRM* in Figure 6d), thus indicating variability in the proportion of hematite and magnetite throughout a relatively constant δ^{56}Fe interval (from 295.80 to 475.10 m). This shows that Fe(II)/Fe(III) variations are not associated with isotopic fractionation, thus arguing for a closed system (i.e., without contribution from an external Fe source). Since one-third of the iron in magnetite is in the Fe(II) form, its origin is yet to be determined. As suggested above from petrographic observations, ferrous iron could originate from the reduction of Fe(III) in ferrihydrite and/or hematite, possibly linked to iron reduction-based metabolic respiration, provided that organic matter was available likely sourced from photoferrotrophs (Zachara et al. 2002; Konhauser, Newman, and Kappler 2005). This also explains the low organic content measured in the Carajás BIFs compared to the carbonate-rich intervals (Rego et al. 2021). Iron isotope studies have consistently shown that microbial DIR produces Fe(II) with a lower ^{56}Fe/^{54}Fe ratio than its ferric substrate (Beard et al. 1999, 2003; Icopini et al. 2004; Crosby et al. 2005, 2007; Tangalos et al. 2010; Fortney et al. 2016). Notably, δ^{56}Fe values in BIFs from Carajás are enriched in ^{56}Fe (Fabre et al. 2011; Rego et al. 2021), making it challenging to use isotopic measurements in bulk rock to directly identify microbial DIR. However, by combining petrographic observations with evidence suggesting that organic matter was likely sourced from photoferrotrophs and recognizing that the low organic content in BIFs likely reflects organic matter remineralization, we cannot exclude the possibility of DIR in the studied samples. Another potential source of ferrous iron is the thermochemical reduction of Fe(III) during late diagenesis or low-grade metamorphism, leading to the formation of inclusion-free magnetite rims.

5.4 | A Model for BIF Deposition in the Carajás Basin

By combining the textural, isotopic, and magnetic data described above, a conceptual model is proposed to summarize the most likely mechanisms involved in the formation of the Carajás BIFs deposit investigated here (Figure 8). As discussed by Rego et al. (2021), the fact that these samples display an unusually elevated positive europium anomaly, combined with the absence of a cerium anomaly, indicates that the Carajás BIFs were formed in an anoxic environment strongly influenced by hydrothermal processes. Considering that anoxygenic photosynthesis was the main mechanism responsible for the oxidation of hydrothermally derived Fe^{+2} into ferrihydrite (Rego et al. 2021), we suggest based on our petrographic observations that this oxidation process was intimately linked with the sorption of hydrothermally derived dissolved silica onto the surfaces of ferric hydroxides to form cell-like features (e.g., Schad et al. 2022) and eventually sink from the surface ocean onto the seafloor (e.g., "iron shuttle" mechanism of Fischer and Knoll 2009). Ferrihydrite has a high surface area and high reactivity due in part to its complex surface (Michel et al. 2007) and therefore can easily interact with aqueous silica. During this interaction, silica binding with the Fe–O sites of ferrihydrite would prevent polymerization resulting in the co-precipitation of iron and

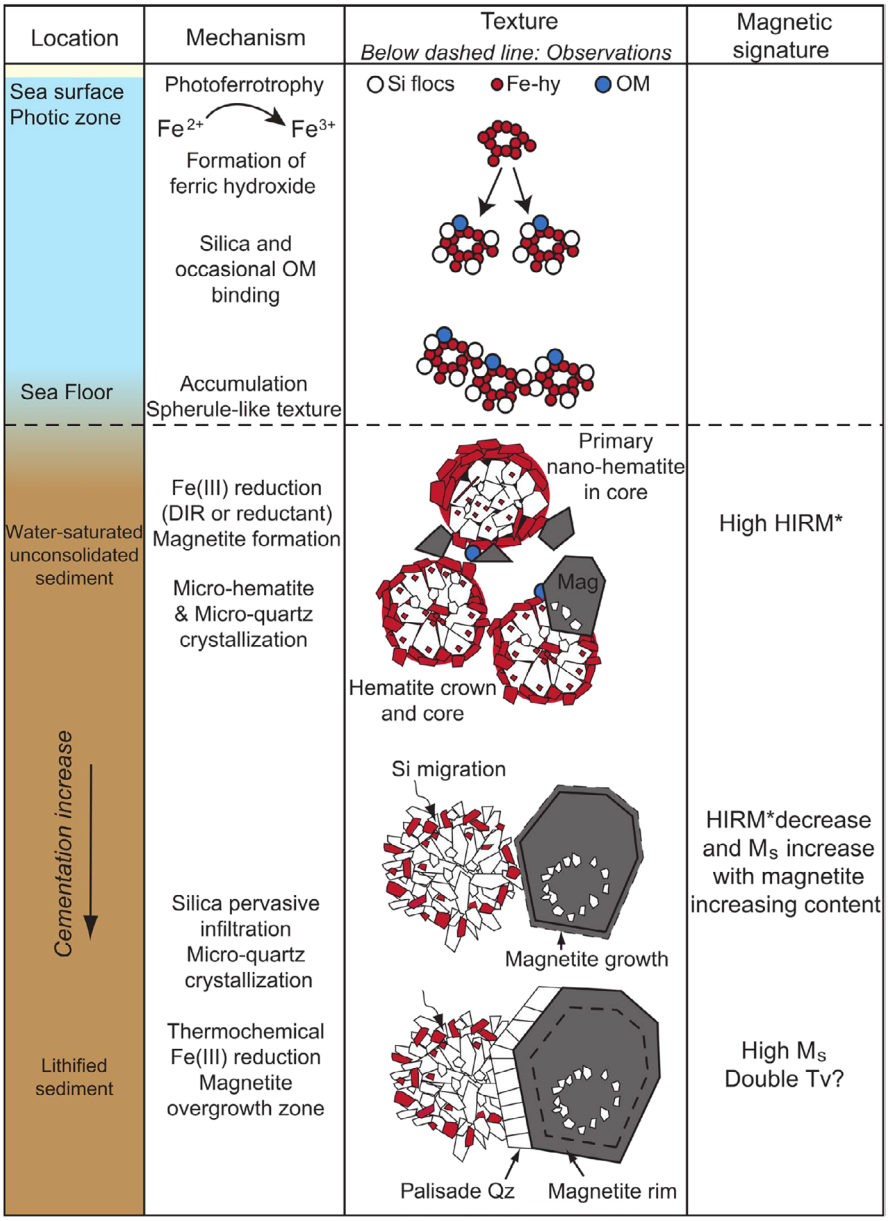

FIGURE 8 | Conceptual model of the crystallization pathways of Fe-oxides and quartz forming the Carajás BIFs deposit (see text for discussion).

silica (e.g., Schulz et al. 2022). Furthermore, the presence of an Si coating could stabilize the underlying ferrihydrite particles, preserving them as a nanophase and preventing dissolution and recrystallization within the water column (Engel et al. 2023). In addition to Si–OH, organic compounds (OM) are also known to readily bind to the surface of ferrihydrite (Engel et al. 2023). In that case, assemblages of Fe(III)-Si-OM gel clusters would fall at the sediments interface, the Si–Fe-rich assemblages behaving as a gel from which microcrystalline quartz and nanocrystalline hematite can crystallize. During this early diagenetic stage, dehydration-induced formation of microcrystalline hematite at the expense of iron hydroxides can also take place. The association of silica and hematite can therefore explain the occurrence of nanoparticles of hematite in the Si-spherules, thus arguing that the 100–500 nm large H1s and H1s(re) may represent the most pristine Fe-oxides present in the Carajás BIFs. The presence of these ferric oxides throughout the studied sequence is further confirmed by the magnetic parameter HIRM*, with high values being proportional to the concentration of hematite forming the BIFs. In this scenario, assemblages of Fe(III)-Si-OM gel clusters might have accumulated at the sediment–water interface until the organic matter was eventually respired by microbial DIR. As Fe(III) undergoes reductive dissolution, the silica is released and can precipitate locally as microcrystalline quartz.

The widespread occurrence of significant quantities of magnetite crystals is attested by the high M_s reported throughout all the BIF section. Magnetite is ubiquitous and overprints the primary hematite–silica layering and honeycomb texture, suggesting that ferric iron is reduced back to Fe(II). Finally, a late diagenetic and/or low-grade metamorphic overprint is proposed based on the observation of pervasive silicification of the matrix and palisade quartz (Figures 2e–i, 3c and 5b). As the degree of Si remobilization increases, silica can migrate pervasively throughout the hematite H1m matrix, leading to silicification of the matrix and local precipitation as palisade quartz along magnetite margins. This stage of silicification of the matrix could have occurred during the second stage of magnetite formation as inclusion-free,

overgrowth zones via thermochemical Fe(III) reduction, which can account for the non-stoichiometric (and double) Verwey transition behavior of some samples revealed by thermomagnetic curves. Further investigations are needed to better understand the underlying causes and implications of this feature.

6 | Conclusions

Our integrated approach, combining high-resolution microscopic observations with bulk rock magnetic techniques, provided comprehensive insights into the crystallization pathways and magnetic properties of the Carajás BIFs. Our findings challenge previous assertions of hematite predominance in these BIFs, demonstrating magnetite as the main Fe-oxide in the majority of the studied lithofacies. The absence of martite indicates that hematite formed after an Fe-oxyhydroxide precursor intimately linked with silica as indicated by primary Si-spherules containing nano-scale H1s hematite. The positive and homogeneous δ^{56}Fe values in the BIFs support the role of anoxygenic photosynthesis attending initial Fe oxidation in the water column (Rego et al. 2021). We argue that microbially induced reduction of hematite likely resulted in the formation of a first generation of magnetite. This early diagenetic stage of magnetite formation was followed by a temperature-controlled stage, characterized by the appearance of rims in different magnetite grains. The occurrence of non-stoichiometric behavior of Verwey transition in samples showing the most advanced stage of diagenetic re-equilibration suggests that Verwey transition's distribution may represent a promising tool for evaluating the crystallization pathways of magnetite in BIFs.

Acknowledgments

We would like to acknowledge the Fundação de Amparo à Pesquisa do Estado de São Paulo (FAPESP) for its financial support through grants: 2015/16235-2, 2019/12132-5, and 2021/10949-4. Special thanks are extended to the Paleomagnetism group and all the IPGP staff, to Stephan Borensztajn for providing access to the SEM and FEG facilities, to France Lagroix for her guidance on MPMS operation, to Samia Hidalgo for her assistance in facilitating access to their lab for our sample preparation, and to Sophie Nowak (and Université Paris Cité) for her support with DRX analyses. We also thank Sônia Alonso and Josias Batista for their invaluable assistance with sample logistics at the University of São Paulo. Finally, we extend our gratitude to Editor Roger Buick, Subject Editor Andreas Kappler, and the three anonymous reviewers for their insightful comments and suggestions, which greatly improved this manuscript.

Conflicts of Interest

The authors declare no conflicts of interest.

Data Availability Statement

The supporting information contains supporting figures and a table related to this manuscript. Raw data from magnetic and DRX measurements are available online at: doi.org/10.6084/m9.figshare.25733718.

References

Beard, B. L., C. M. Johnson, L. Cox, H. Sun, K. H. Nealson, and C. Aguilar. 1999. "Iron Isotope Biosignatures." *Science* 285: 1889–1892.

Beard, B. L., C. M. Johnson, J. L. Skulan, K. H. Nealson, L. Cox, and H. Sun. 2003. "Application of Fe Isotopes to Tracing the Geochemical and Biological Cycling of Fe." *Chemical Geology* 195: 87–117.

Beukes, N. J., and J. Gutzmer. 2008. "Origin and Paleoenvironmental Significance of Major Iron Formations at the Archean-Paleoproterozoic Boundary." *Reviews in Economic Geology* 15: 5–47.

Bloemendal, J., J. W. King, F. R. Hall, and S. J. Doh. 1992. "Rock Magnetism of Late Neogene and Pleistocene Deep-Sea Sediments-Relationship to Sediment Source, Diagenetic Processes, and Sediment Lithology." *Journal of Geophysical Research - Solid Earth* 97: 4361–4375.

Braterman, P. S., A. G. Cairns-Smith, and R. W. Sloper. 1983. "Photooxidation of Hydrated Fe^{2+}—Significance for Banded Iron Formations." *Nature* 303: 163–164.

Cabral, A. R., B. Bühn, A. A. Seabra Gomes, H. F. Galbiatti, B. Lehmann, and S. Halder. 2017. "Multiple Sulfur Isotopes From the Neoarchean Serra Sul Black Shale, Carajás Mineral Province, Northern Brazil." *Journal of South American Earth Sciences* 79: 377–383.

Cabral, A. R., R. A. Creaser, T. Nägler, et al. 2013. "Trace-Element and Multi-Isotope Geochemistry of Late-Archean Black Shales in the Carajás Iron-Ore District, Brazil." *Chemical Geology* 362: 91–104.

Cairns-Smith, A. G. 1978. "Precambrian Solution Photochemistry, Inverse Segregation, and Banded Iron Formations." *Nature* 276: 807–808.

Carlut, J., A. Isambert, H. Bouquerel, et al. 2015. "Low Temperature Magnetic Properties of the Late Archean Boolgeeda Iron Formation (Hamersley Group, Western Australia): Environmental Implications." *Frontiers in Earth Science* 3: 18.

Chang, L., D. Heslop, A. P. Roberts, D. Rey, and K. J. Mohamed. 2015. "Discrimination of Biogenic and Detrital Magnetite Through a Double Verwey Transition Temperature." *Journal of Geophysical Research - Solid Earth* 121: 3–14.

Cloud, P. 1973. "Paleoecological Significance of Banded Iron-Formation." *Economic Geology* 68: 1135–1143.

Craddock, P. R., and N. Dauphas. 2011. "Iron and Carbon Isotope Evidence for Microbial Iron Respiration Throughout the Archean." *Earth and Planetary Science Letters* 303: 121–132.

Crosby, H. A., C. M. Johnson, E. E. Roden, and B. L. Beard. 2005. "Coupled Fe(II)-Fe(III) Electron and Atom Exchange as a Mechanism for Fe Isotope Fractionation During Dissimilatory Iron Oxide Reduction." *Environmental Science & Technology* 39: 6698–6704.

Crosby, H. A., E. E. Roden, C. M. Johnson, and B. L. Beard. 2007. "The Mechanisms of Iron Isotope Fractionation Produced During Dissimilatory Fe(III) Reduction by *Shewanella putrefaciens* and *Geobacter sulfurreducens*." *Geobiology* 5: 169–189.

Czaja, A. D., K. M. J. Van, B. L. Beard, and C. M. Johnson. 2018. "A Multistage Origin for Neoarchean Layered Hematite-Magnetite Iron Formation From the Weld Range, Yilgarn Craton, Western Australia." *Chemical Geology* 488: 125–137.

Day, R., M. Fuller, and V. A. Schmidt. 1977. "Hysteresis Properties of Titanomagnetites: Grain-Size and Compositional Dependence." *Physics of the Earth and Planetary Interiors* 13: 260–267.

Dekkers, M. J., and J. H. Linssen. 1989. "Rockmagnetic Properties of Fine-Grained Natural Low-Temperature Hematite With Reference to Remanence Acquisition Mechanisms in Red Beds." *Geophysical Journal International* 99: 1–18.

Dunlop, D. J. 2002. "Theory and Application of the Day Plot (M_{rs}/M_s Versus H_{cr}/H_c) 1. Theoretical Curves and Tests Using Titanomagnetite Data." *Journal of Geophysical Research* 107: 2056.

Dunlop, D. J., and O. Özdemir. 1997. *Rock Magnetism: Fundamentals and Frontiers*. Cambridge, UK: Cambridge University Press.

Engel, M., V. Noël, S. Pierce, et al. 2023. "Structure and Composition of Natural Ferrihydrite Nano-Colloids in Anoxic Groundwater." *Water Research* 238: 119990.

Evans, M., and F. Heller. 2003. *Environmental Magnetism: Principles and Applications of Enviromagnetics*. Amsterdam, the Netherlands: Elsevier.

Fabre, S., A. Nédélec, F. Poitrasson, H. Strauss, C. Thomazo, and A. Nogueira. 2011. "Iron and Sulphur Isotopes From the Carajás Mining Province (Pará, Brazil): Implications for the Oxidation of the Ocean and the Atmosphere Across the Archaean-Proterozoic Transition." *Chemical Geology* 289: 124–139.

Fischer, W. W., and A. H. Knoll. 2009. "An Iron Shuttle for Deepwater Silica in Late Archean and Early Paleoproterozoic Iron Formation." *Geological Society of America Bulletin* 121: 222–235.

Fortney, N. W., S. He, B. J. Converse, et al. 2016. "Microbial Fe(III) Oxide Reduction Potential in Chocolate Pots Hot Spring, Yellowstone National Park." *Geobiology* 14: 255–275.

Frank, U., and N. R. Nowaczyk. 2008. "Mineral Magnetic Properties of Artificial Samples Systematically Mixed From Haematite and Magnetite." *Geophysical Journal International* 175: 449–461.

Gibbs, A. K., K. R. Wirth, W. K. Hirata, and W. K. Olszewski. 1986. "Age and Composition of the Grão Pará Group Volcanics, Serra dos Carajás." *Revista Brasileira de Geociencias* 16: 201–211.

Halama, M., E. D. Swanner, K. O. Konhauser, and A. Kappler. 2016. "Evaluation of Siderite and Magnetite Formation in BIFs by Pressure-Temperature Experiments of Fe(III) Minerals and Microbial Biomass." *Earth and Planetary Science Letters* 450: 243–253.

Heimann, A., C. M. Johnson, B. L. Beard, et al. 2010. "Fe, C and O Isotope Compositions of Banded Iron Formation Carbonates Demonstrate a Major Role for Dissimilatory Iron Reduction in ~2.5 Ga Marine Environments." *Earth and Planetary Science Letters* 294: 8–18.

Huston, D. L., and G. A. Logan. 2004. "Barite, BIFs and Bugs: Evidence for the Evolution of the Earth's Early Hydrosphere." *Earth and Planetary Science Letters* 220, no. 41: 55.

Icopini, G. A., A. D. Anbar, S. S. Ruebush, M. Tien, and S. L. Brantley. 2004. "Iron Isotope Fractionation During Microbial Reduction of Iron: The Importance of Adsorption." *Geology* 32: 205–208.

Jackson, M. J., and B. Moskowitz. 2021. "On the Distribution of Verwey Transition Temperatures in Natural Magnetites." *Geophysical Journal International* 224: 1314–1325.

Johnson, C. M., E. E. Roden, S. A. Welch, and B. L. Beard. 2005. "Experimental Constraints on Fe Isotope Fractionation During Magnetite and Fe Carbonate Formation Coupled to Dissimilatory Hydrous Ferric Oxide Reduction." *Geochimica et Cosmochimica Acta* 69: 963–993.

Johnson, J. E., J. R. Muhling, J. Cosmidis, B. Rasmussen, and A. S. Templeton. 2018. "Low-Fe(III) Greenalite Was a Primary Mineral From Neoarchean Oceans." *Geophysical Research Letters* 45, no. 7: 3182–3192.

Justo, A. P., E. L. Dantas, M. Bau, F. H. Freitas-Silva, R. V. Santos, and J. H. D. Schorscher. 2020. "Paleobasinal to Band-Scale REE+Y Distribution in Iron Formations From Carajás, Amazon Craton, Brazil." *Ore Geology Reviewes* 127: 103750.

Kappler, A., C. Pasquero, K. O. Konhauser, and D. K. Newman. 2005. "Deposition of Banded Iron Formations by Anoxygenic Phototrophic Fe(II)-oxidizing Bacteria." *Geology* 33: 865–868.

Klein, C. 2005. "Some Precambrian Banded Iron-Formations (BIFs) From Around the World: Their Age, Geologic Setting, Mineralogy, Metamorphism, Geochemistry, and Origin." *American Mineralogist* 90: 1473–1499.

Klein, C., and E. A. Ladeira. 2002. "Petrography and Geochemistry of the Least Altered Banded Iron-Formation of the Archean Carajás Formation, Northern Brazil." *Economic Geology* 97: 643–651.

Kletetschka, G., and J. Wasilewski. 2002. "Grain Size Limit for SD Hematite." *Physics of the Earth and Planetary Interiors* 129: 173–179.

Köhler, I., K. O. Konhauser, D. Papineau, A. Bekker, and A. Kappler. 2013. "Biological Carbon Precursor to Diagenetic Siderite With Spherical Structures in Iron Formations." *Nature Communications* 4: 1741.

Konhauser, K. O., T. Hamade, R. Raiswell, et al. 2002. "Could Bacteria Have Formed the Precambrian Banded Iron Formations?" *Geology* 30: 1079–1082.

Konhauser, K. O., D. K. Newman, and A. Kappler. 2005. "The Potential Significance of Microbial Fe(III) Reduction During Deposition of Precambrian Banded Iron Formations." *Geobiology* 3: 167–177.

Konhauser, K. O., N. J. Planavsky, D. S. Hardisty, et al. 2017. "Iron Formations: A Global Record of Neoarchean to Palaeoproterozoic Environmental History." *Earth-Science Reviews* 172: 140–177.

Kruiver, P. P., C. G. Langereis, M. J. Dekkers, and W. Krijgsman. 2003. "Rock-Magnetic Properties of Multicomponent Natural Remanent Magnetization in Alluvial Red Beds (NE Spain)." *Geophysical Journal International* 153: 317–332.

Krymsky, R. S., M. J. B. Macambira, J. M. Lafon, and G. S. Estumano. 2007. "Uranium–Lead Dating Method at the Pará-Iso Isotope Geology Laboratory, UFPA. Belém—Brazil." *Anais da Academia Brasileira de Ciências* 79: 115–128.

Li, Y.-L., K. O. Konhauser, A. Kappler, and X.-L. Hao. 2013. "Experimental Low-Grade Alteration of Biogenic Magnetite Indicates Microbial Involvement in Generation of Banded Iron Formations." *Earth and Planetary Science Letters* 361: 229–237.

Lindenmayer, Z. G., J. H. Laux, and J. B. G. Teixeira. 2001. "Considerações Sobre a Origem das Formações Ferríferas da Formação Carajás, Serra dos Carajás." *Revista Brasileira de Geociencias* 31: 21–28.

Liu, P., A. M. Hirt, D. Schüler, et al. 2019. "Numerical Unmixing of Weakly and Strongly Magnetic Minerals: Examples With Synthetic Mixtures of Magnetite and Hematite." *Geophysical Journal International* 217: 280–287.

Liu, Q., V. Barrón, J. Torrent, H. Qin, and Y. Yu. 2010. "The Magnetism of Micro-Sized Hematite Explained." *Physics of the Earth and Planetary Interiors* 183: 387–397.

Liu, Q. S., A. P. Roberts, J. Torrent, C. S. Horng, and J. C. Larrasoaña. 2007. "What Do the HIRM and S-Ratio Really Measure in Environmental Magnetism?" *Geochemistry, Geophysics, Geosystems* 8, no. 9: 1525–2027.

Lovley, D. R., and E. J. P. Ohillips. 1986. "Organic Matter Mineralization With Reduction of Ferric Iron in Anaerobic Sediments." *Applied and Environmental Microbiology* 51: 683–689.

Lovley, D. R., J. F. Stolz, G. L. Nord, and E. J. P. Philips. 1987. "Anaerobic Production of Magnetite by a Dissimilatory Iron-Reducing Microorganism." *Nature* 330: 252–254.

Macambira, J. B. 2003. "O Ambiente Deposicional da Formação Carajás e Uma Proposta de Modelo Evolutivo Para a Bacia Grão Pará." Universidade Estadual de Campinas, Ph.D. Thesis, 217p.

Macambira, J. B., and A. Schrank. 2002. "Químio-Estratigrafia e Evolução dos Jaspilítos da Formação Carajás (PA)." *Revista Brasileira de Geociencias* 32: 567–578.

Machado, N., Z. G. Lindenmayer, T. E. Krogh, and D. Lindenmayer. 1991. "U–Pb Geochronology of Archean Magmatism and Basement Reactivation in the Carajás Área, Amazon Shield, Brazil." *Precambrian Research* 49: 329–354.

Martins, P. L. G., C. L. B. Toledo, A. M. Silva, F. Chemale Jr., C. Archer, and L. M. Assis. 2022. "Chemostratigraphy of the Carajás Banded Iron Formation, Brazil: A Record of Neoarchean Ocean Chemistry." *Gondwana Research* 105: 217–242.

Martins, P. L. G., C. L. B. Toledo, A. M. Silva, F. Chemale Jr., J. O. S. Santos, and L. M. Assis. 2017. "Neoarchean Magmatism in the Southeastern Amazonian Craton, Brazil: Petrography, Geochemistry and Tectonic Significance of Basalts From the Carajás Basin." *Precambrian Research* 302: 340–357.

Michel, F. M., L. Ehm, S. M. Antao, et al. 2007. "The Structure of Ferrihydrite, a Nanocrystalline Material." *Science* 316: 1726–1729.

Nie, N. X., N. Dauphas, and R. C. Greenwood. 2017. "Iron and Oxygen Isotope Fractionation During Iron UV Photo-Oxidation: Implications for Early Earth and Mars." *Earth and Planetary Science Letters* 458: 179–191.

O'Reilly, W. 1984. *Rock and Mineral Magnetism*. New York, NY: Blackie.

Posth, N. R., I. Köhler, E. D. Swanner, et al. 2013. "Simulating Precambrian Banded Iron Formation Diagenesis." *Chemical Geology* 362: 66–73.

Rasmussen, B., B. Krapež, and D. B. Meier. 2014. "Replacement Origin for Hematite in 2.5 Ga Banded Iron Formation: Evidence for Postdepositonal Oxidation of Iron-Bearing Minerals." *Geological Society of America Bulletin* 126: 438–446.

Rasmussen, B., J. R. Muhling, and B. Krapež. 2021. "Greenalite and Its Role in the Genesis of Early Precambrian Iron Formations—A Review." *Earth-Science Reviews* 217: 103613.

Rasmussen, B., J. R. Muhling, A. A. Suvorova, and B. Krapež. 2016. "Dust to Dust: Evidence for the Formation of "Primary" Hematite Dust in Banded Iron Formations via Oxidation of Iron Silicate Nanoparticles." *Precambrian Research* 284: 49–63.

Rego, E. S., V. Busigny, S. V. Lalonde, et al. 2021. "Anoxygenic Photosynthesis Linked to Neoarchean Iron Formations in Carajás (Brazil)." *Geobiology* 19, no. 4: 326–341.

Rego, E. S., V. Busigny, S. V. Lalonde, C. Rossignol, M. Babinski, and P. Philippot. 2023. "Low-Phosphorus Concentrations and Important Ferric Hydroxide Scavenging in Archean Seawater." *PNAS Nexus* 2: 1–7.

Ribeiro da Luz, R., and J. K. Crowley. 2012. "Morphological and Chemical Evidence of Stromatolitic Deposits in the 2.75 Ga Carajás Banded Iron Formation, Brazil." *Earth and Planetary Science Letters* 355: 60–72.

Rosière, C. A., F. J. Baars, J. C. S. Seoane, et al. 2006. "Structure and Iron Mineralisation of the Carajás Province." *Applied Earth Science* 115, no. 4: 126–133.

Rossignol, C., P. Y. J. Antonio, F. Narduzzi, et al. 2022. "Unravelling One Billion Years of Geological Evolution of the Southeastern Amazonian Craton From Detrital Zircon Analyses." *Geoscience Frontiers* 13: 101202.

Rossignol, C., E. S. Rego, P. Philippot, et al. 2023. "Neoarchean Environments Associated With the Emplacement of a Large Igneous Province: Insights From the Carajás Basin, Amazon Craton." *Journal of South American Earth Sciences* 130: 104574.

Schad, M., J. M. Byrne, L. K. ThomasArrigo, R. Kretzschmar, K. O. Konhauser, and A. Kappler. 2022. "Microbial Fe Cycling in a Simulated Precambrian Ocean Environment: Implications for Secondary Mineral (Trans)formation and Deposition During BIF Genesis." *Geochimica et Cosmochimica Acta* 331: 165–191.

Schmidt, P. W., and D. A. Clark. 1994. "Palaeomagnetic and Magnetic Anisotropy of Proterozoic Banded-Iron Formations and Iron Ores of the Hamersley Basin, Western Australia." *Precambrian Research* 69: 133–155.

Schulz, K., L. K. ThomasArrigo, R. Kaegi, and R. Kretzschmar. 2022. "Stabilization of Ferrihydrite and Lepidrocrite by Silicate During Fe(II)-catalyzed Mineral Transformation: Impact on Particle Morphology and Silicate Distribution." *Environmental Science & Technology* 56: 5929–5938.

Smirnov, A. V. 2009. "Grain Size Dependence of Low-Temperature Remanent Magnetization in Natural and Synthetic Magnetite: Experimental Study." *Earth, Planets and Space* 61: 119–124.

Smith, A. J. B., and N. J. Beukes. 2023. "The Paleoenvironmental Implications of Pre-Great Oxidation Manganese Deposition in the Mesoarchean Ijzermijn Iron Formation Bed, Mozaan Group, Pongola Supergroup, South Africa." *Precambrian Research* 384: 106922.

Smith, A. J. B., N. J. Beukes, and J. Gutzmer. 2013. "The Composition and Depositional Environments of Mesoarchean Iron Formations of the West Rand Group of the Witwatersrand Supergroup, South Africa." *Economic Geology* 108: 111–134.

Sumita, I., T. Hatakeyama, A. Yoshihara, and Y. Hamano. 2001. "Paleomagnetism of Late Archean Rocks of Hamersley Basin, Western Australia and the Paleointensity at Early Proterozoic." *Physics of the Earth and Planetary Interiors* 128: 223–241.

Sun, S., K. O. Konhauser, A. Kappler, and Y.-L. Li. 2015. "Primary Hematite in Neoarchean to Paleoproterozoic Oceans." *GSA Bulletin* 127: 850–861.

Tangalos, G. E., B. L. Beard, C. M. Johnson, et al. 2010. "Microbial Production of Isotopically Light Iron(II) in a Modern Chemically Precipitated Sediment and Implications for Isotopic Variations in Ancient Rocks." *Geobiology* 8: 197–208.

Tauxe, L. 2010. *Essentials of Paleomagnetism*. Berkeley, CA: University of California Press.

Teixeira, N. L., F. A. Caxito, C. A. Rosière, et al. 2017. "Trace Elements and Isotope Geochemistry (C, O, Fe, Cr) of the Cauê Iron Formation, Quadrilátero Ferrífero, Brazil: Evidence for Widespread Microbial Dissimilatory Iron Reduction at the Archean/Paleoproterozoic Transition." *Precambrian Research* 298: 39–55.

Tolbert, G. E., J. W. Tremaine, G. C. Melcher, and C. B. Gomes. 1971. "The Recently Discovered Serra dos Carajás Iron Deposits, Northern Brazil." *Economic Geology* 66: 985–994.

Tompkins, L. A., and D. R. Cowan. 2001. "Opaque Mineralogy and Magnetic Properties of Selected Banded Iron-Formations, Hamersley Basin, Western Australia." *Australian Journal of Earth Sciences* 48: 427–437.

Tosca, N. J., S. Guggenheim, and P. K. Pufahl. 2016. "An Authigenic Origin for Precambrian Greenalite: Implications for Iron Formation and the Chemistry of Ancient Seawater." *Bulletin of the Geological Society of America* 128: 511–530.

Trendall, A. F. 2002. "The Significance of Iron-Formation in the Precambrian Stratigraphic Record." *International Association of Sedimentologists* 33: 33–66.

Trendall, A. F., M. A. S. Basei, J. R. De Laeter, and D. R. Nelson. 1998. "SHRIMP U–Pb Constraints on the Age of the Carajás Formation, Grão Pará Group, Amazon Craton." *Journal of South American Earth Sciences* 11: 265–277.

Van Zuilen, M. A., A. Lepland, J. Teranes, J. Finarelli, M. Wahlen, and G. Arrhenius. 2003. "Graphite and Carbonates in the 3.8 Ga Old Isua Supracrustal Belt, Southern West Greenland." *Precambrian Research* 126: 331–348.

Vuillemin, A., M. Morlock, A. Paskin, et al. 2023. "Authigenic Minerals Reflect Microbial Control on Pore Waters in a Ferruginous Analogue." *Geochemical Perspectives Letters* 28: 20–26.

Zachara, J. M., R. K. Kukkadapu, J. K. Fredrickson, Y. A. Gorby, and S. C. Smith. 2002. "Biomineralization of Poorly Crystalline Fe(III) Oxides by Dissimilatory Metal Reducing Bacteria (DMRB)." *Geomicrobiology Journal* 19: 179–207.

Supporting Information

Additional supporting information can be found online in the Supporting Information section.